

# 1 Blue-shifted deep ocean currents in the equatorial

## 2 Indian Ocean

3 P. Amol<sup>\*1</sup> · Vineet Jain<sup>2</sup> · S. G. Aparna<sup>2</sup>

4  
5 the date of receipt and acceptance should be inserted later

6 **Abstract** Spectra from two decades of zonal current data at  $\sim 4000$  m in the  
7 central and western equatorial Indian Ocean show a shift in the dominant fre-  
8 quencies from the west to the east. The 120–180-day period is stronger at  $77^\circ\text{E}$  ,  
9 the 60–120-day period at  $83^\circ\text{E}$ , and the 30–90-day period at  $93^\circ\text{E}$ . The weakening  
10 of lower frequencies near the eastern boundary can be explained using theoretical  
11 ray paths of Kelvin waves and reflected Rossby waves. The equatorial Kelvin wave  
12 forced by winds reflects from the eastern boundary as Rossby waves with different  
13 meridional modes. After reflection, the low (high) frequency Rossby beams travel  
14 a larger (shorter) distance before reaching the bottom, thereby creating a shadow  
15 zone, a region with low wave energy, between the ray path and the eastern bound-  
16 ary. The shift in frequency with longitude is not evident in the top 1000 m, where  
17 the current is dominated by the semi-annual cycle.

---

\* Corresponding author

<sup>1</sup> CSIR-National Institute of Oceanography, Regional Centre, Visakhapatnam, India

<sup>2</sup> CSIR-National Institute of Oceanography, Dona Paula, Goa, India

18 **Keywords** Equatorial Ocean · Bottom currents · Indian Ocean · Rossby waves ·  
19 Kelvin waves · Ray path

## 20 **1 Introduction**

21 Observations from the equatorial Indian Ocean show energetic current fluctuations  
22 in the deeper waters (Luyten and Swallow 1976; Eriksen 1980; O'Neill and Luyten  
23 1984; Ponte and Luyten 1990; Dengler and Quadfasel 2002). The zonal currents  
24 throughout the water column are characterised by complex vertical structures with  
25 time scales longer than a month and are trapped within few degrees of the equator.  
26 Several attempts were made to explain the energy available for the sustenance of  
27 such deep ocean currents, and one of the possible reasons is the direct transmission  
28 of wind-forced energy into deeper waters.

29 Numerical solutions have shown that periodic zonal winds generate a well-  
30 defined Kelvin beam that propagates both eastwards and downwards (McCreary  
31 1984; Rothstein et al. 1985). The Kelvin beam reflects from the eastern boundary  
32 as a Rossby beam, which has a steeper ray path that can reach the bottom of the  
33 ocean at seasonal time scales. The signatures of these beams are evident in the ob-  
34 servations from the equatorial Indian Ocean. Luyten and Roemmich (1982) showed  
35 that the mid-depth zonal currents in the western equatorial Indian ocean were  
36 dominated by the semi-annual cycle. They suggested that these fluctuations were  
37 caused by equatorially trapped Kelvin waves and first meridional mode Rossby  
38 waves. Huang et al. (2018) arrived at the same conclusion in the central and east-  
39 ern equatorial Indian Ocean using an oceanic reanalysis product. They showed  
40 the enhancement of the semi-annual cycle and the associated phase propagation

41 in the intermediate depths (200–1500 m) of the central equatorial Indian Ocean  
42 were caused by reflected first-mode Rossby waves.

43 The transmission of wind-forced energy into the deeper waters will, however,  
44 be affected by the presence of a strong pycnocline (Philander 1978). Gent and  
45 Luyten (1985) showed that there was considerable reflection of energy from the  
46 pycnocline, which prevented the transmission of wind-forced energy into deeper  
47 waters. Their study only described a single reflection, and a complete picture  
48 involves re-reflections of energy from the surface (Kessler and McCreary 1993).  
49 With each reflection, a small fraction of energy would leak into the deep ocean.  
50 In addition, Rothstein et al. (1985) suggested that the vertical mixing could cause  
51 model solutions to lose their beam-like characteristics, which is probably why the  
52 simulations, like that by Philander and Pacanowski (1981), show strong trapping  
53 of energy near the surface. Some studies have also shown that random fluctuations  
54 in density could cause waves to decay in the direction of energy propagation more  
55 rapidly (Tang and Mysak 1976; Mysak 1978). If the beam weakens with depth  
56 owing to damping and variations in density, can the wind energy flux reach the  
57 bottom of the ocean and impact the deep ocean circulation?

58 In this study, we use spectra of deep zonal currents ( $\sim 4000$  m) obtained from  
59 the data collected during 2000–2020 to show signatures of wind-driven circulation  
60 in the near-bottom currents. The dominant frequencies blue shift with longitude  
61 — the 120–180-day period is stronger at  $77^\circ\text{E}$ , the 60–120-day period at  $83^\circ\text{E}$ ,  
62 and the 30–90-day period at  $93^\circ\text{E}$  — and this shift in frequency can be explained  
63 using theoretical ray paths of Kelvin and Rossby waves. The signatures of these  
64 waves propagating downwards as equatorial beams are also evident in the current  
65 observations from the near-surface and intermediate depths.

66 The rest of the paper is organised as follows. Sec. 2 describes the data used in  
67 this study. The spectra of the  $\sim 4000$  m zonal currents are shown in Sec. 3. The  
68 effect of ray paths and shadow zones in causing a shift towards higher frequencies in  
69 the eastern Indian Ocean is detailed out in Sec. 4. Sec. 5 summarises and concludes  
70 the study.

## 71 2 Data and Methods

72 We used data from the deep-sea equatorial mooring programme, which is under  
73 Ocean Observation Network (OON) programme of ESSO-Indian National Centre  
74 for Ocean Information Services (INCOIS), India (Jain et al. 2021). The currents  
75 were measured at three locations:  $77^\circ\text{E}$ ,  $83^\circ\text{E}$ , and  $93^\circ\text{E}$  (Fig. 1a). The data from  
76 the top 1400 m were obtained from Acoustic Doppler Current Profilers (ADCP),  
77 and the vertical and temporal resolution was 16 m and one hour, respectively.  
78 Recording current meters (RCMs) with the same temporal resolution were used  
79 to measure currents at  $\sim 1000$ ,  $\sim 2000$  m and  $\sim 4000$  m depths. The depth of the  
80 water column at these three locations vary between 4400 and 4700 m. The data  
81 were collected from 2000–2020 and were discontinuous, with gaps ranging from  
82 few days to few years. The data at  $93^\circ\text{E}$  were available only till 2014. The details  
83 of mooring configuration and data availability are available in Jain et al. (2021).

84 As there were extensive gaps in the ADCP data, we used the Lomb-Scargle  
85 periodogram to compute the spectra (Lomb 1976; Scargle 1982). Unlike the fast  
86 Fourier transform, this approach computes the power spectral density of unevenly  
87 spaced data sets or, in this case, data sets with gaps. The periodogram was nor-  
88 malised using residuals of data around the constant reference model. The signifi-

89 cance test or the false alarm probability was computed using the bootstrap method  
90 (see VanderPlas (2018) for details related to Lomb-Scargle periodogram and false  
91 alarm probability).

92 The wind data from 2000–2016 were obtained by merging QuikSCAT and AS-  
93 CAT satellite data products (<https://coastwatch.pfeg.noaa.gov/>). The tem-  
94 perature and salinity data for computing Brunt-Väisälä frequency profile were  
95 from the World Ocean Atlas (Boyer et al. 2018).

### 96 **3 Spectra of the bottom currents**

97 In this section, we show basic statistics and spectra for the near-bottom zonal  
98 currents at  $\sim 4000$  m. The magnitude of currents at  $\sim 4000$  m ranges from  $-12$  to  $12$   
99  $\text{cm s}^{-1}$  and the mean flow is close to zero at all locations (Fig. 1b–d). The standard  
100 deviation is  $4.2 \text{ cm s}^{-1}$  at  $77^\circ\text{E}$  and drops to  $3.2 \text{ cm s}^{-1}$  at  $93^\circ\text{E}$ . In comparison,  
101 the maximum magnitude is greater than  $100 \text{ cm s}^{-1}$  for near-surface currents and  
102 decreases to  $30\text{--}50 \text{ cm s}^{-1}$  at intermediate depths of  $200\text{--}1000$  m (Jain et al. 2021).  
103 Similarly, the mean flow is eastward ( $15\text{--}60 \text{ cm s}^{-1}$ ) for the near-surface current  
104 and close to zero for the intermediate current. The near-bottom currents at all  
105 three locations are de-correlated.

106 The Lomb-periodogram for the bottom currents shows that the dominant fre-  
107 quencies blue-shifts with longitude (Fig. 2a–c). The lower frequencies are stronger  
108 at the western mooring ( $77^\circ\text{E}$ ), while the higher frequencies are stronger at the  
109 eastern mooring ( $93^\circ\text{E}$ ). At  $77^\circ\text{E}$ , the seasonal cycles, like the 120-day, 160-day  
110 and 180-day period, dominate (Fig. 2a). The 90-day and 60-day peaks are also  
111 evident, but they are weaker compared to the seasonal cycles. At  $83^\circ\text{E}$ , the 60–

112 130-day band dominates with the strongest peaks observed in the 90–100-day band  
113 (Fig. 2b). The amplitude of these peaks is weaker compared to the seasonal cycle  
114 observed at 77°E. At 93°E, the strongest peaks are observed between 30–70-days  
115 (Fig. 2c). There are no significant peaks evident between 90–140 days. The 150-day  
116 and the semi-annual peaks are weaker but comparable to the intraseasonal peri-  
117 ods. Even though the semi-annual cycle is evident at all locations, the amplitude  
118 weakens eastwards.

119 The spectra also shows a frequency shift with depth at 93°E (Fig. 2f). The 30–  
120 50-day peak, which is the dominant band at 4000 m, weakens at 2000 m. At this  
121 depth, the 90-day peak is the strongest. The intraseasonal periods further weakens  
122 at 1000 m and the seasonal cycles, like 120-day, become stronger. Between 150–500  
123 m, the semi-annual cycle is the strongest.

124 The surface circulation in the equatorial Indian Ocean is known for its strong  
125 semi-annual cycle. The spectra shows that the cycle is the strongest between 500–  
126 1500 m (200–500 m) depth at 77°E and 83°E (93°E, Fig. 2d-i). Huang et al.  
127 (2018) also found a maximum variance for the semi-annual harmonic in this depth  
128 range. Though the semi-annual cycle is strong near the surface at all locations  
129 (Fig. 2d,e), the amplitude of the higher frequencies becomes comparable at 93°E  
130 (Fig. 2f). The relatively weak semi-annual period and strong intraseasonal periods  
131 at 93°E at intermediate depths were reported by Chen et al. (2020) using ADCP  
132 data from 2015–2019.

## 133 4 Equatorial beams

134 In this section, we use the ray paths derived from ‘equatorial beam theory’ (Mc-  
135 Creary 1984) along with observations from the equatorial moorings to explain the  
136 shift in dominant frequencies observed in the bottom currents. We first show how  
137 the ray paths and shadow zones (or low wave energy zones) of large-scale waves  
138 vary based on the property of the wave and the medium (Section 4.1). We then  
139 compare the theoretical ray paths with observed spectra and highlight the role of  
140 beams in causing a shift in dominant frequencies along the longitude (Section 4.2).

### 141 4.1 The shifting shadow zones

142 We define shadow zones as regions in the equatorial ocean where large-scale waves  
143 are not detected due to the presence of continental boundaries or topographical  
144 obstructions, like ridges and islands. The area of the shadow zone depends on  
145 the frequency of waves (Fig. 3d), stratification (Fig. 3e), the width of the basin  
146 (Fig. 3f), and in the case of Rossby waves, the meridional mode number (Fig. 3c).

147 Based on Wentzel-Kramers-Brillouin (WKB) approximation, the slope of the  
148 ray path is given by  $\omega/N_b(z)$  for Kelvin waves and  $(2n + 1)\omega/N_b(z)$  for Rossby  
149 waves, where  $\omega$  is the frequency and  $N_b(z)$  is the background Brunt-Väisälä fre-  
150 quency profile. The climatological  $N_b(z)$  profiles are averaged from 45°E–98°E  
151 along the equator. The details regarding the approximations for computing the  
152 ray path can be found in McCreary (1984).

153 Fig. 3a shows a schematic of beams generated by 150–210-day band winds at  
154 77°E. The  $N_b(z)$  used to calculate the ray path is the annual climatology. The beam  
155 travelling towards the west from the wind source is the incident Rossby wave (only

156 the first meridional mode shown), and the beam travelling towards the east is the  
157 equatorial Kelvin wave. The Kelvin wave also reflects from the eastern boundary  
158 as a first meridional mode Rossby wave. As the wave propagates downwards along  
159 its ray path, its energy would drop and spread owing to wave damping or vertical  
160 mixing. Numerical simulations by [McCreary \(1984\)](#) show that the reflected Rossby  
161 waves from an eastern boundary can cause more energy to propagate into the deep  
162 ocean compared to the directly forced waves generated in an unbounded solution.

163 If the wind blows all along the equator, similar ray paths for each wave can  
164 be plotted at all longitudes. For a given basin size, the region occupied by all  
165 these ray paths (Fig. 3b) will be constrained by the ray paths of the Kelvin wave  
166 and the incident Rossby wave generated near the western and eastern boundaries,  
167 respectively (solid lines in Fig. 3b). For example, the Kelvin wave will be trapped  
168 within the top 250 m of the ocean, and the width of this trapping increases from  
169 west to east based on the slope of the ray path. In this region, the Kelvin wave does  
170 not occur in isolation and can superpose with either the incident or the reflected  
171 Rossby waves. The ray paths of the incident Rossby wave cover a major fraction  
172 of the ocean basin (almost the entire water column in the western Indian Ocean),  
173 whereas the ray paths of the first mode reflected Rossby waves is confined to the  
174 eastern and central Indian Ocean. The grey shaded region is the shadow zone,  
175 which forms below the ray path of the reflected Rossby waves.

176 Higher meridional modes (Fig. 3c) and higher frequencies (Fig. 3d) have steeper  
177 ray paths and smaller shadow zones. Kelvin wave is a single mode wave; hence, af-  
178 ter reflection, only the width of the shadow zone varies with each meridional mode  
179 of the Rossby wave (Fig. 3c). Based on the aforementioned ray path equation,  
180 the shadow zone of the Rossby wave would disappear if the number of meridional

181 modes tends to infinity. However, the equation is an approximation and holds only  
182 for low-frequency, low-wavenumber, inviscid Rossby waves. At higher meridional  
183 modes, there are fewer baroclinic modes that can strongly couple with winds at  
184 seasonal and intraseasonal time scales, and it would be unreasonable to associate  
185 the higher meridional modes with vertical propagation of energy as several baro-  
186 clinic modes must superpose to form beams (McCreary 1984; Mukherjee et al.  
187 2018).

188 If the frequency increases, both the width and the height of the shadow zone  
189 would decrease (Fig. 3d). The decrease in the width of the shadow zone with  
190 frequency explains the observed shift in spectral peaks in the bottom currents (see  
191 Section 4.2 for more details). A similar change in the height of the shadow zone  
192 would cause a shift in the frequency with depth; the lower (higher) frequencies will  
193 be stronger near the surface (bottom). This shift is evident at 93°E mooring, even  
194 though the vertical resolution of the data is very coarse below 500 m (Fig. 2i).

195 The area of the shadow zone also depends on the size of the basin; as the basin  
196 size increases, the width and the height of the shadow zone decreases. For a given  
197 basin size, there is a cut-off period below which the shadow zone will not form.  
198 For 4000 m depth, the cut-off period is  $\sim 135$  days for the Pacific Ocean and  $\sim 50$   
199 days for the Indian Ocean and the Atlantic Ocean. Fig. 3f shows that there is  
200 no shadow zone for the 90-day period in the Pacific Ocean, whose basin width is  
201 much larger than that of the Indian Ocean. At lower frequencies, like the annual  
202 cycle, the beam slope is so small that it takes more than  $\sim 25,000$  km for the beam  
203 to reach 1000 m depth (Rothstein et al. 1985).

204 In general, we can ignore the effect of stratification as they cause only small  
205 changes in the ray path (Fig. 3e). Rossby waves can also reflect from the western

206 boundary or the bottom of the ocean and can create complex structures (McCreary  
207 1984). In the case of bottom reflection, the phase (energy) would propagate down-  
208 wards (upwards).

#### 209 4.2 Observational evidence for beams

210 The observed frequency shift at  $\sim 4000$  m can be explained using the shadow zones  
211 of the reflected Rossby waves from the eastern boundary. Fig. 4 shows ray paths  
212 for both Kelvin and Rossby waves for four periods: 180, 120, 90, and 30 days. The  
213 shadow zone is marked as hatched lines for the fifth meridional mode. The ray  
214 paths are plotted from the eastern and western boundaries as they represent the  
215 extreme case for the directly forced and reflected waves (similar to Fig. 3b). In  
216 reality, the beam path changes based on the location of the wind forcing, which  
217 varies along the equator (Fig. 5). Strong spectral peaks within the vicinity of the  
218 incident or eastern boundary Rossby wave path (orange and solid red lines in  
219 Fig. 4) suggest that the wind forcing is strong in the eastern Indian Ocean. Simi-  
220 larly, strong peaks near the reflected Rossby wave path (green and purple dashed  
221 line) traced using a western boundary Kelvin wave (solid blue line) suggest that  
222 the winds are strong in the western Indian Ocean. Note that, unless specifically  
223 mentioned, we discuss only the Kelvin and first mode Rossby ray paths here, and  
224 the fifth mode Rossby ray paths are shown only for reference.

225 The 180-day ray path in Fig. 4a follows the result obtained by Huang et al.  
226 (2018). The beam path of the first-mode reflected Rossby and Kelvin waves co-  
227 incides with enhanced spectral power in the upper 1500 m (Fig. 4). Huang et al.  
228 (2018) showed that the variance explained in this depth range extended only till

229 65°E, west of which the variance is weaker. The significant power observed below  
230 1500 m could be due to the higher-order meridional modes or vertical mixing,  
231 which could weaken and broaden the beam both vertically and meridionally (Mc-  
232 Creary 1984).

233 The wind spectra show that the semi-annual cycle is strong along the en-  
234 tire basin, and the maximum amplitude is observed between 60°E–80°E (Fig. 5).  
235 Therefore, the peak would be expected somewhere between the reflected Rossby  
236 (dashed curve) and the incident Rossby wave path. The maximum amplitude for  
237 the 180-day signal is observed at ~680 m at 77°E and 200 m at 93°E.

238 The 120-day ray path is similar to the semi-annual cycle (Fig. 4b). The spectral  
239 power enhances along the Kelvin and first-mode reflected Rossby ray paths. As  
240 both Kelvin and Rossby ray paths cross each other between 200–600 m at 83°E, it  
241 is difficult to separate them at this depth range. At 77°E, the maximum amplitude  
242 is observed at 2000 m depth and is in the vicinity of the first-mode reflected  
243 Rossby wave path. The 120-day wind spectra show a bimodal structure with power  
244 weakening in the central Indian Ocean (Fig. 5). This weakening of power is also  
245 evident between the reflected and incident Rossby ray paths (Fig. 4b).

246 The 90-day power enhances along Rossby ray paths generated by winds near  
247 the eastern (solid line) and the western (dashed line) Indian Ocean (Fig. 4c). The  
248 strongest power is observed at 1000 m at 77°E, which lies within the vicinity of the  
249 incident Rossby ray path. Like the 120 days, the winds in 90–100-day band also  
250 have a bimodal structure: the ~95 day is strong in the eastern Indian Ocean and  
251 ~90 day is strong in the western Indian Ocean (Fig. 5). Han (2005) showed that  
252 even though the winds are relatively weak, the Indian Ocean selectively responds  
253 to the 90-day forcing, owing to the resonance excitation of second-baroclinic mode

254 waves. The resonance is more concentrated towards the eastern Indian Ocean  
255 because the westward propagating Rossby wave is slower compared to the eastward  
256 propagating Kelvin wave (Han et al. 2011). Nevertheless, the 90-day period peaks  
257 at 4000 m (2000 m) at 83°E (77°E) along the reflected Rossby ray path, which  
258 suggests that the winds in the western Indian Ocean are also important in driving  
259 the currents at deeper depths.

260 The 30-day period is the minimum period of the Rossby wave, and there is no  
261 shadow zone for this period (Fig. 4d). The minimum period is an approximation  
262 and would vary based on the speed of the first baroclinic mode Kelvin wave.  
263 For  $c = 3 \text{ ms}^{-1}$ , the minimum period is 30.4 days. The beam generation for  
264 Rossby waves at higher frequencies, in general, is unlikely, because these waves are  
265 dispersive and cannot retain their coherency as wave packets. The non-dispersive  
266 Kelvin waves, however, can reach the bottom of the ocean and enhance the power  
267 east of 80°E. The presence of the Central Indian Ridge at 75°E creates a local  
268 shadow zone for high-frequency Kelvin waves generated by winds in the western  
269 Indian Ocean. The spectra show that the winds in the 30–60-day band are stronger  
270 between 60–90°E (Fig. 5), and it is the energy from the wind forcing at  $\sim 60^\circ\text{E}$   
271 that reaches the bottom at 93°E (see thin blue line in Fig. 4d). Though beams  
272 generated between 55–58°E can also reach the bottom, they will be obstructed by  
273 the Ninety East Ridge.

274 In summary, the energy from the spectra is the weakest in the shadow zones  
275 of the reflected Rossby waves, and the blue shift in dominant frequencies of the  
276 bottom currents is linked to the shift in the width of the shadow zone (Fig. 3d).  
277 The dominant frequency also changes with depth because of the change in the  
278 height of the shadow zone and is evident at 93°E (Fig. 2i).

## 279 **5 Discussion**

280 The surface circulation in the equatorial Indian Ocean is dominated by the semi-  
281 annual cycle. The eastward jets that occur during the boreal spring and autumn  
282 are known as the Wyrтки Jets (Wyrтки 1973). These jets are known to be driven by  
283 zonal winds with current speeds that can peak more than  $2 \text{ m s}^{-1}$ . The impact of  
284 these winds are stronger in the top 200–300 m below which strong upward phase  
285 propagation is evident (Jain et al. 2021; McPhaden et al. 2015). Our study shows  
286 that the dominance of the semi-annual cycle does not extend till the bottom of  
287 the ocean, particularly in the eastern Indian Ocean. Near the bottom, the lower  
288 frequencies are stronger at  $77^\circ\text{E}$  and become weaker towards the east. The shift  
289 in frequencies is caused by the vertical propagation of energy generated by surface  
290 winds. The wind-forced Kelvin waves reflect from the eastern boundary as Rossby  
291 waves and propagate downwards. The ray path of Rossby waves has a larger slope  
292 compared to Kelvin wave and can reach the bottom of the ocean even at seasonal  
293 time scales. At higher frequencies, there are no Rossby waves, but the ray path of  
294 the Kelvin waves is steeper and can reach the bottom of the ocean.

295 Based on the linear-wave theory, one may expect weak spectral power in the  
296 shadow zones and anything outside would be a complex superposition of several  
297 modes generated by winds all along the equatorial region. The spectral analy-  
298 sis shows that the strong spectral power roughly coincides with the beam path  
299 of the first-mode reflected Rossby waves (Fig. 4). This result is consistent with  
300 that shown in earlier studies (Luyten and Roemmich 1982; Huang et al. 2018;  
301 Zanowski and Johnson 2019). The observed amplification of wave energy along  
302 the first-mode reflected Rossby ray path could be due to the following reasons.

303 For vertical propagation of energy, several baroclinic modes of a meridional mode  
304 should superpose, but higher meridional modes have only fewer baroclinic modes  
305 that can strongly couple with winds and hence are weaker. The effect of the even  
306 meridional modes would be negligible because the Hermite polynomials are anti-  
307 symmetric and have a zero-crossing at the equator. In addition, higher modes have  
308 shorter wavelengths and can be diffused more easily by friction.

309 The spectral analysis shows that there is significant energy evident in the  
310 shadow zone of the first mode ray path. For example, the 180-day peak is one  
311 of the dominant peaks for the bottom currents at  $93^\circ\text{E}$  (Fig. 2c). It is difficult  
312 to attribute the energy observed in the shadow zone to higher meridional modes  
313 because it is possible that the wave energy could spread out along the ray path  
314 due to vertical mixing (McCreary 1984; Rothstein et al. 1985). Also, the 180-  
315 day period is the strongest period in the equatorial Indian Ocean, and the energy  
316 would penetrate deeper compared to that from other periods before it is completely  
317 dissipated.

318 The analysis presented here is not without caveats. The ray path is calculated  
319 based on the WKB approximation, which is not valid in the upper few hundred  
320 meters because of the sharp changes in the density profile. For the beam to pene-  
321 trate the thermocline, the vertical scale of the oscillations should be much smaller  
322 than the background variations of  $N_b^2$ . A typical vertical wavelength for the first  
323 mode is 4900 m (60 cm equivalent depth), and this wavelength is almost seven  
324 times more than the wavelength of waves that can freely pass through the ther-  
325 mocline (Moore and Philander 1977; Boyd 2018). In addition, Gent and Luyten  
326 (1985) showed that for an equivalent depth between 1 cm and 1 m only 10–20%  
327 of the energy could pass through the thermocline. As the ocean surface acts like

328 a rigid lid, one must also consider the effects of re-reflection; with each reflec-  
329 tion, more fraction of energy would penetrate the thermocline. In addition, the  
330 wind-forcing extends deep into the mixed layer, and its impact on energy transfer  
331 through turbulent processes is not well understood.

332 The downward propagation of energy can also be modified by the presence  
333 of mid-oceanic ridges and islands. They can create a local shadow zone, cause  
334 re-reflections, and affect the resonance amplitude of the baroclinic modes. For  
335 example, [Chen et al. \(2020\)](#) showed that Maldives islands could cause abrupt  
336 changes in the amplitude of the equatorial intermediate current. However, as the  
337 islands lie on the nodes of the first four baroclinic modes, the resonance amplitude  
338 is not affected.

339 In spite of the above-mentioned limitations, the spectra of the zonal currents  
340 show an enhancement of energy along the Kelvin and Rossby ray paths, suggesting  
341 that the surface forcing from the winds reaches the bottom of the ocean. The  
342 transmission of energy is evident for both seasonal and intraseasonal time scales,  
343 which explains the observed frequency shift near the bottom of the ocean.

344 Deep ocean currents are known to be driven by differences in water density.  
345 They play an important role in the transport of water masses across the ocean  
346 basin and significantly impact climate scale processes. Earlier studies have shown  
347 signatures of Madden-Julian Oscillations in the deeper oceans ([Matthews et al.](#)  
348 [2007](#); [Webber et al. 2014](#)). Unlike the surface circulation, the spatial distribution  
349 of the intraseasonal frequencies and climate modes, such as El Niño and Indian  
350 Ocean Dipole, near the bottom would be determined by the ray path of these  
351 large-scale waves. The downward propagation of energy by surface winds would  
352 also play an important role in the deep ocean biogeochemistry.

353 **Acknowledgements** The authors thank Julian P. McCreary for sharing his insights on the  
354 equatorial beam theory and D. Shankar for his critical comments. The support from the CSIR-  
355 NIO mooring group (V. Fernando, N P Satelkar, S. T. Khalap, S. Ghatkar, P. A. Tari, and  
356 M. G. Gaonkar), ship cell members (M S Kerkar, S P Vernekar and A C D'Souza), officers,  
357 crew, and seamen from various cruises is gratefully acknowledged. The mooring operations  
358 were carried out on the research vessels O R V Sagar Kanya, R V Sindhu Sadhana, and T D  
359 V Sagar Nidhi. The authors also thank V. S. N. Murty and his colleagues for overseeing the  
360 deep-sea mooring programme from 2000–2017. This is CSIR-NIO contribution ?????.

## 361 **Declarations**

### 362 Funding

363 Financial support for this project was provided by Ministry of Earth Sciences  
364 (MoES), India via their Ocean Observation Network (OON) programme and by  
365 Council of Scientific and Industrial Research (CSIR).

### 366 Conflict of interest

367 The authors declare that they have no conflict of interest.

### 368 Data availability

369 The ocean current data are available from <https://incois.gov.in/essdp/>. The  
370 wind data were obtained <https://coastwatch.pfeg.noaa.gov/>. The temperature  
371 and salinity data are from <https://www.ncei.noaa.gov/products/world-ocean-atlas>.

372 Code availability

373 Python packages (astropy, numpy, scipy, matplotlib, and netCDF4) were used for  
374 analysis and graphics.

375 Authors' contributions

376 – P. Amol: Conceived and designed the study; acquired, analysed, and inter-  
377 preted the data; drafted the article.

378

379 – V. Jain: Acquired and analysed the data; drafted the article; implemented com-  
380 puter programs.

381

382 – S. G. Aparna: Processed and organised the data; reviewed and edited the ar-  
383 ticle.

384

## 385 **References**

386 Boyd JP (2018) Dynamics of the equatorial ocean. Springer-Verlag Berlin Heidelberg, <https://doi.org/10.1007/978-3-662-55476-0>

388 Boyer TP, Garcia HE, Locarnini RA, Zweng MM, Mishonov AV, Reagan JR, Weathers KA,  
389 Baranova OK, Paver CR, Seidov D, Smolyar IV (2018) World Ocean Atlas 2018. NOAA  
390 National Centers for Environmental Information [https://www.ncei.noaa.gov/archive/  
391 accession/NCEI-WOA18](https://www.ncei.noaa.gov/archive/accession/NCEI-WOA18)

392 Chen G, Han W, Zhang X, Liang L, Xue H, Huang K, He Y, Li J, Wang D (2020) Determination  
393 of Spatiotemporal Variability of the Indian Equatorial Intermediate Current. Journal of  
394 Physical Oceanography 50(11):3095–3108, <https://doi.org/10.1175/JP0-D-20-0042.1>

- 395 Dengler M, Quadfasel D (2002) Equatorial deep jets and abyssal mixing in the Indian  
396 Ocean. *Journal of Physical Oceanography* 32(4):1165–1180, [https://doi.org/10.1175/  
397 1520-0485\(2002\)032<1165:EDJAAM>2.0.CO;2](https://doi.org/10.1175/1520-0485(2002)032<1165:EDJAAM>2.0.CO;2)
- 398 Eriksen CC (1980) Evidence for a continuous spectrum of equatorial waves in the Indian Ocean.  
399 *Journal of Geophysical Research: Oceans* 85(C6):3285–3303, [https://doi.org/10.1029/  
400 JC085iC06p03285](https://doi.org/10.1029/JC085iC06p03285)
- 401 Gent PR, Luyten JR (1985) How much energy propagates vertically in the equatorial  
402 oceans? *Journal of Physical Oceanography* 15(7):997–1007, [https://doi.org/10.1175/  
403 1520-0485\(1985\)015<0997:HMEPVI>2.0.CO;2](https://doi.org/10.1175/1520-0485(1985)015<0997:HMEPVI>2.0.CO;2)
- 404 Han W (2005) Origins and dynamics of the 90-day and 30–60-day variations in the equatorial  
405 Indian Ocean. *Journal of Physical Oceanography* 35(5):708–728, [https://doi.org/10.  
406 1175/JP02725.1](https://doi.org/10.1175/JP02725.1)
- 407 Han W, McCreary JP, Masumoto Y, Vialard J, Duncan B (2011) Basin resonances in the  
408 equatorial Indian Ocean. *Journal of Physical Oceanography* 41(6):1252–1270, [https://  
409 doi.org/10.1175/2011JP04591.1](https://doi.org/10.1175/2011JP04591.1)
- 410 Huang K, McPhaden MJ, Wang D, Wang W, Xie Q, Chen J, Shu Y, Wang Q, Li J, Yao J (2018)  
411 Vertical propagation of middepth zonal currents associated with surface wind forcing in  
412 the equatorial Indian Ocean. *Journal of Geophysical Research: Oceans* 123(10):7290–7307,  
413 <https://doi.org/10.1029/2018JC013977>
- 414 Jain V, Amol P, Aparna S, Fernando V, Kankonkar A, Murty V, Almeida A, Sardar AA,  
415 Khalap S, Satelkar N, et al. (2021) Two decades of current observations in the equatorial  
416 Indian Ocean. *Journal of Earth System Science* 130(2):1–8, [https://doi.org/10.1007/  
417 s12040-021-01568-4](https://doi.org/10.1007/s12040-021-01568-4)
- 418 Kessler WS, McCreary JP (1993) The annual wind-driven Rossby wave in the subthermocline  
419 equatorial Pacific. *Journal of Physical Oceanography* 23(6):1192–1207, [https://doi.org/  
420 10.1175/1520-0485\(1993\)023<1192:TAWDRW>2.0.CO;2](https://doi.org/10.1175/1520-0485(1993)023<1192:TAWDRW>2.0.CO;2)
- 421 Lomb NR (1976) Least-squares frequency analysis of unequally spaced data. *Astrophysics and*  
422 *space science* 39(2):447–462, <https://doi.org/10.1007/BF00648343>
- 423 Luyten JR, Roemmich DH (1982) Equatorial currents at semi-annual period in the In-  
424 dian Ocean. *Journal of Physical Oceanography* 12(5):406–413, <https://doi.org/10.1175/>

- 425       1520-0485(1982)012<0406:ECASAP>2.0.CO;2
- 426 Luyten JR, Swallow J (1976) Equatorial undercurrents. *Deep Sea Research and Oceanographic*  
427       Abstracts 23(10):999–1001, [https://doi.org/10.1016/0011-7471\(76\)90830-5](https://doi.org/10.1016/0011-7471(76)90830-5)
- 428 Matthews AJ, Singhruck P, Heywood KJ (2007) Deep ocean impact of a Madden-Julian Oscil-  
429       lation observed by Argo floats. *Science* 318(5857):1765–1769, [https://doi.org/10.1126/](https://doi.org/10.1126/science.1147312)  
430       [science.1147312](https://doi.org/10.1126/science.1147312)
- 431 McCreary JP (1984) Equatorial beams. *Journal of Marine Research* 42(2):395–430, [https:](https://doi.org/10.1357/002224084788502792)  
432       [//doi.org/10.1357/002224084788502792](https://doi.org/10.1357/002224084788502792)
- 433 McPhaden MJ, Wang Y, Ravichandran M (2015) Volume transports of the W yrkti jets and  
434       their relationship to the Indian Ocean Dipole. *Journal of Geophysical Research: Oceans*  
435       120(8):5302–5317, <https://doi.org/10.1002/2015JC010901>
- 436 Moore DW, Philander SGH (1977) Modelling of the tropical ocean circulation, *The Sea*, vol 6.  
437       John Wiley & Sons, New York
- 438 Mukherjee A, Shankar D, Chatterjee A, Vinayachandran P (2018) Numerical simulation of  
439       the observed near-surface east india coastal current on the continental slope. *Climate*  
440       Dynamics 50(11):3949–3980, <https://doi.org/10.1007/s00382-017-3856-x>
- 441 Mysak LA (1978) Wave propagation in random media, with oceanic applications. *Reviews of*  
442       Geophysics 16(2):233–261, <https://doi.org/10.1029/RG016i002p00233>
- 443 O’Neill K, Luyten JR (1984) Equatorial velocity profiles. Part II: Zonal component. *Journal*  
444       of Physical Oceanography 14(12):1842–1852, [https://doi.org/10.1175/1520-0485\(1984\)](https://doi.org/10.1175/1520-0485(1984)014<1842:EVPPIZ>2.0.CO;2)  
445       [014<1842:EVPPIZ>2.0.CO;2](https://doi.org/10.1175/1520-0485(1984)014<1842:EVPPIZ>2.0.CO;2)
- 446 Philander S (1978) Forced oceanic waves. *Reviews of Geophysics* 16(1):15–46, [https://doi.](https://doi.org/10.1029/RG016i001p00015)  
447       [org/10.1029/RG016i001p00015](https://doi.org/10.1029/RG016i001p00015)
- 448 Philander S, Pacanowski R (1981) Response of equatorial oceans to periodic forcing.  
449       *Journal of Geophysical Research: Oceans* 86(C3):1903–1916, [https://doi.org/10.1029/](https://doi.org/10.1029/JC086iC03p01903)  
450       [JC086iC03p01903](https://doi.org/10.1029/JC086iC03p01903)
- 451 Ponte RM, Luyten J (1990) Deep velocity measurements in the western equatorial In-  
452       dian Ocean. *Journal of Physical Oceanography* 20(1):44–52, [https://doi.org/10.1175/](https://doi.org/10.1175/1520-0485(1990)020<0044:DVMITW>2.0.CO;2)  
453       [1520-0485\(1990\)020<0044:DVMITW>2.0.CO;2](https://doi.org/10.1175/1520-0485(1990)020<0044:DVMITW>2.0.CO;2)

- 454 Rothstein LM, Moore DW, McCreary JP (1985) Interior reflections of a periodically forced  
455 equatorial Kelvin wave. *Journal of Physical Oceanography* 15(7):985–996, [https://doi.  
456 org/10.1175/1520-0485\(1985\)015<0985:IROAPF>2.0.CO;2](https://doi.org/10.1175/1520-0485(1985)015<0985:IROAPF>2.0.CO;2)
- 457 Scargle JD (1982) Studies in astronomical time series analysis. ii-statistical aspects of spectral  
458 analysis of unevenly spaced data. *The Astrophysical Journal* 263:835–853, [https://doi.  
459 org/10.1086/160554](https://doi.org/10.1086/160554)
- 460 Sindhu B, Suresh I, Unnikrishnan A, Bhatkar N, Neetu S, Michael G (2007) Improved bathy-  
461 metric datasets for the shallow water regions in the Indian Ocean. *Journal of Earth System  
462 Science* 116(3):261–274, <https://doi.org/10.1007/s12040-007-0025-3>
- 463 Tang C, Mysak L (1976) A note on “Internal waves in a randomly stratified fluid”. *Jour-  
464 nal of Physical Oceanography* 6(2):243–246, [https://doi.org/10.1175/1520-0485\(1976\)  
465 006<0243:ANOWIA>2.0.CO;2](https://doi.org/10.1175/1520-0485(1976)006<0243:ANOWIA>2.0.CO;2)
- 466 VanderPlas JT (2018) Understanding the Lomb–Scargle periodogram. *The Astrophysical Jour-  
467 nal Supplement Series* 236(1):16
- 468 Webber BG, Matthews AJ, Heywood KJ, Kaiser J, Schmidtko S (2014) Seaglider observations  
469 of equatorial Indian Ocean Rossby waves associated with the Madden-Julian Oscillation.  
470 *Journal of Geophysical Research: Oceans* 119(6):3714–3731, [https://doi.org/10.1002/  
471 2013JC009657](https://doi.org/10.1002/2013JC009657)
- 472 Wyrтки K (1973) An equatorial jet in the indian ocean. *Science* 181(4096):262–264, [10.1126/  
473 science.181.4096.262](https://doi.org/10.1126/science.181.4096.262)
- 474 Zanowski H, Johnson GC (2019) Semiannual variations in 1,000-dbar equatorial indian ocean  
475 velocity and isotherm displacements from argo data. *Journal of Geophysical Research:  
476 Oceans* 124(12):9507–9516, <https://doi.org/10.1029/2019JC015342>

477 **Figure captions**

478 **Fig. 1:** (a) Map showing the mooring locations. The background is the bathymetry  
479 from [Sindhu et al. \(2007\)](#). The inset shows map of north Indian Ocean. The red  
480 dashed line is the region of interest. Zonal currents at 4000 m at (b) 77°E, (c)  
481 83°E, and (d) 93°E.

482 **Fig. 2** Normalized Lomb periodogram of zonal currents at 4000 m depth: (a)  
483 77°E, (b) 83°E, and (c) 93°E. The dashed horizontal line shows the 1% false alarm  
484 probability. The gray shaded region highlights the shift in dominant frequencies  
485 from west to east. (d)–(f) Same as (a)–(c) but for currents at 60 m (black) and 150–  
486 500 m (red). The spectra for the 150–500 m current is computed after averaging  
487 the current over this depth range. Note that the ordinate does not have the same  
488 limits. (g)–(i) Normalized Lomb periodogram of zonal currents with depth. As  
489 the difference in power is large between the surface and bottom currents, the  
490 periodogram is smoothed and plotted in log scale to highlight the shift in dominant  
491 frequency with depth. The hatched area is equivalent to the gray shaded region in  
492 panels (a)–(c).

493 **Fig. 3** Schematic of the ray paths in the equatorial Indian Ocean. (a) The shaded  
494 regions depict beams generated by 150–210-day zonal wind at 77°E: Kelvin wave  
495 (blue), incident Rossby wave (red), and reflected Rossby wave (green). The thick  
496 solid lines show the corresponding 180-day ray path. (b) The region occupied  
497 by all the ray paths of a 180-day wave when the wind blows along the entire  
498 equatorial Indian Ocean. The incident (reflected) Rossby wave occupies the blue  
499 (green) shaded region. Both Kelvin wave and incident (reflected) Rossby wave  
500 occupy the purple (blue) region. The solid lines show the ray paths generated at

501 the boundaries. As waves cannot be generated by winds beyond these boundaries,  
 502 the ray paths act as the lower limit below which the wave cannot be detected.  
 503 The grey shaded region is the shadow zone where no ray paths reach. (c) Ray  
 504 paths of reflected Rossby waves for different meridional modes generated by a 180-  
 505 day Kelvin wave from the western boundary. Higher modes have steeper slopes  
 506 and smaller shadow zones. (d) Ray paths of reflected Rossby waves generated by  
 507 Kelvin waves with different frequencies. The area of the shadow zone decreases  
 508 with increasing frequency. (e) Ray paths of 180-day Kelvin waves and reflected  
 509 Rossby waves with different  $N_b^2$  profiles to show the effect of stratification on the  
 510 shadow zone. The differences are negligible between the summer (red) and the  
 511 winter (blue) profiles. (f) The 90-day Kelvin wave ray paths from the western  
 512 boundary of the Indian Ocean and the maritime continent. The reflected Rossby  
 513 wave is evident only in the Indian Ocean. In the Pacific Ocean, the Kelvin wave  
 514 reaches 4000 m without generating reflected Rossby waves because of the larger  
 515 basin size. The arrowheads in all panels indicate the direction of the ray paths,  
 516 and the ray paths are shown only for the first meridional mode except in panel  
 517 (c).

518 **Fig 4** The panels show ray paths for Kelvin and Rossby waves for four different  
 519 periods: a) 180 day, b) 120 day, c) 90 day, and d) 30 day. The shaded color represent  
 520 the log of the normalized periodogram of the zonal currents. Blue solid (thin) line  
 521 is the Kelvin ray path generated from the western boundary ( $59.5^\circ\text{E}$ ). The orange  
 522 and red solid lines are Rossby beams generated at the eastern boundary for mode  
 523 1 and 5, respectively. The green and purple dashed lines are the Rossby beams  
 524 generated after the Kelvin wave (blue solid) reflects from the eastern boundary.  
 525 The dark brown region is the bathymetry and the hatched region is the shadow

526 zone for the mode 5 reflected Rossby waves. The white vertical line/circles show  
527 data availability. The lines represent ADCP data and the circles represent data  
528 from current meters. The ray paths are calculated based on the WKB theory. The  
529 colour levels for the periodogram are not the same for all panels.

530 **Fig. 5** Figure showing periodogram of winds at the equator. The power is plot-  
531 ted in log scale after detrending and applying a Hamming window. The ordinate  
532 is periods and the abscissa is the longitude. The wind data used to calculate the  
533 periodogram extends from 2000–2016.

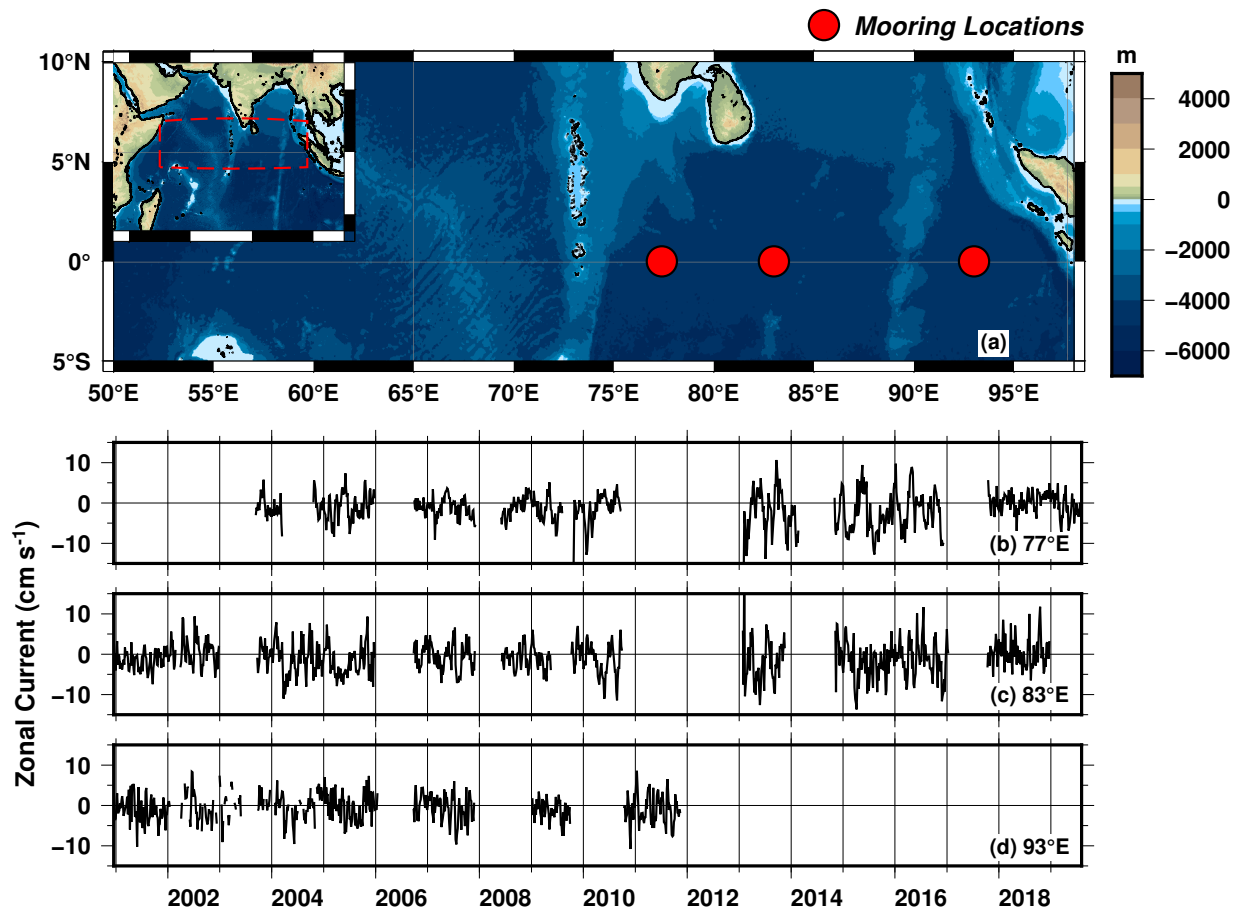


**Fig. 1** (a) Map showing the mooring locations. The background is the bathymetry from [Sindhu et al. \(2007\)](#). The inset shows map of north Indian Ocean. The red dashed line is the region of interest. Zonal currents at 4000 m at (b) 77°E, (c) 83°E, and (d) 93°E.

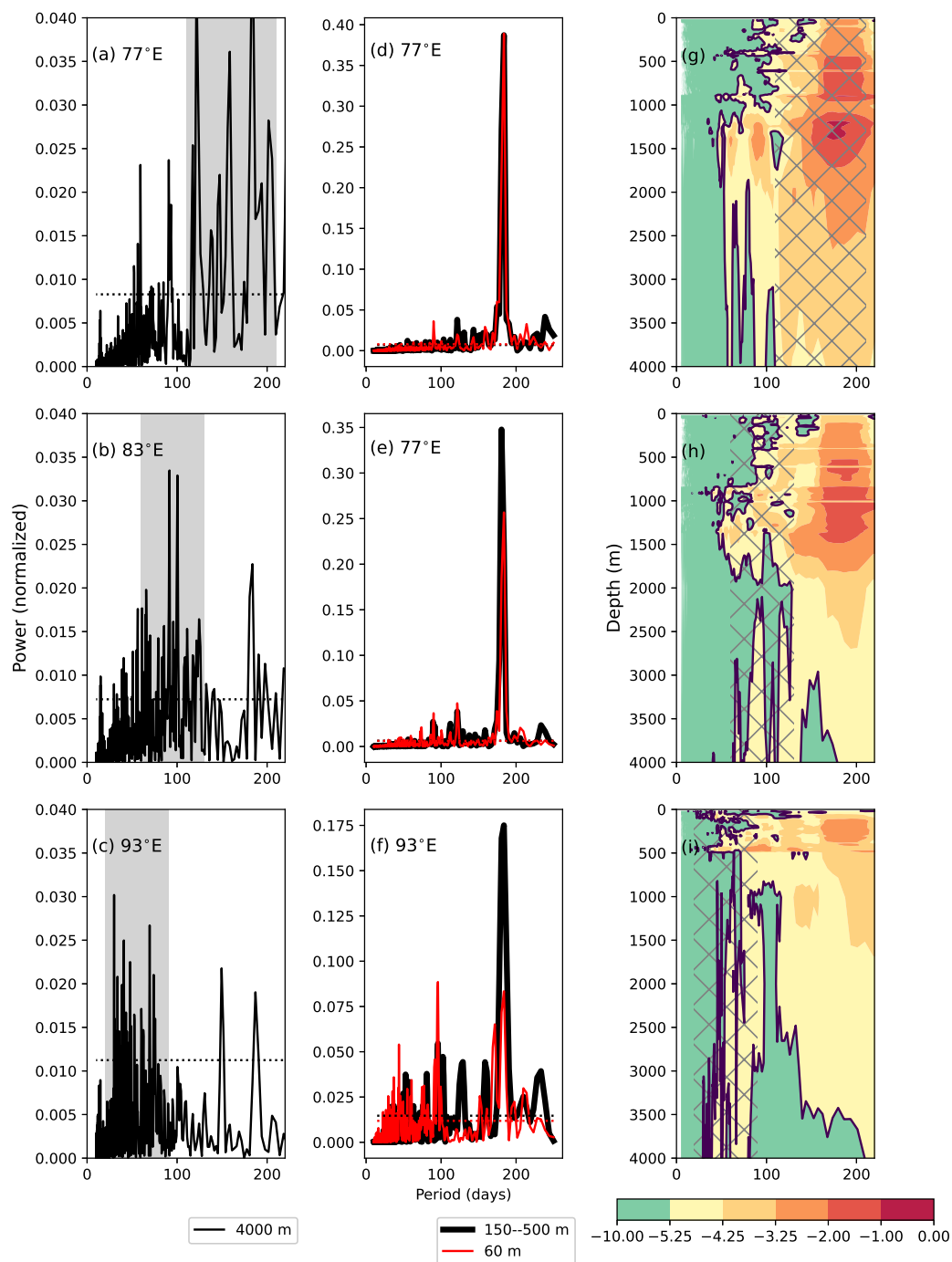


**Fig. 2** Normalized Lomb periodogram of zonal currents at 4000 m depth: (a) 77°E, (b) 83°E, and (c) 93°E. The dashed horizontal line shows the 1% false alarm probability. The gray shaded region highlights the shift in dominant frequencies from west to east. (d)–(f) Same as (a)–(c) but for currents at 60 m (black) and 150–500 m (red). The spectra for the 150–500 m current is computed after averaging the current over this depth range. Note that the ordinate does not have the same limits. (g)–(i) Normalized Lomb periodogram of zonal currents with depth. As the difference in power is large between the surface and bottom currents, the periodogram is smoothed and plotted in log scale to highlight the shift in dominant frequency with depth. The hatched area is equivalent to the gray shaded region in panels (a)–(c).

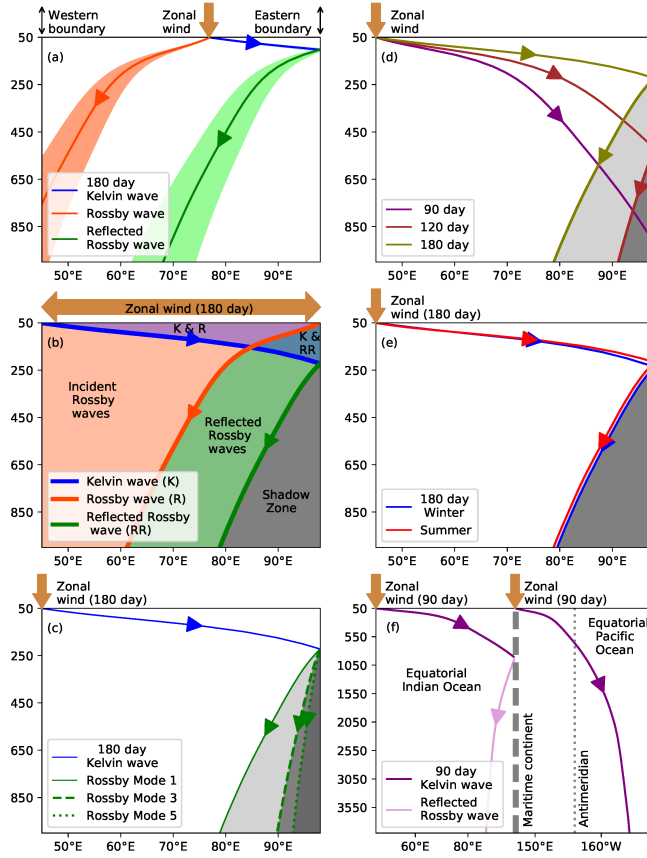


**Fig. 3** Schematic of the ray paths in the equatorial Indian Ocean. (a) The shaded regions depict beams generated by 150–210-day zonal wind at 77°E: Kelvin wave (blue), incident Rossby wave (red), and reflected Rossby wave (green). The thick solid lines show the corresponding 180-day ray path. (b) The region occupied by all the ray paths of a 180-day wave when the wind blows along the entire equatorial Indian Ocean. The incident (reflected) Rossby wave occupies the blue (green) shaded region. Both Kelvin wave and incident (reflected) Rossby wave occupy the purple (blue) region. The solid lines show the ray paths generated at the boundaries. As waves cannot be generated by winds beyond these boundaries, the ray paths act as the lower limit below which the wave cannot be detected. The grey shaded region is the shadow zone where no ray paths reach. (c) Ray paths of reflected Rossby waves for different meridional modes generated by a 180-day Kelvin wave from the western boundary. Higher modes have steeper slopes and smaller shadow zones. (d) Ray paths of reflected Rossby waves generated by Kelvin waves with different frequencies. The area of the shadow zone decreases with increasing frequency. (e) Ray paths of 180-day Kelvin waves and reflected Rossby waves with different  $N_b^2$  profiles to show the effect of stratification on the shadow zone. The differences are negligible between the summer (red) and the winter (blue) profiles. (f) The 90-day Kelvin wave ray paths from the western boundary of the Indian Ocean and the maritime continent. The reflected Rossby wave is evident only in the Indian Ocean. In the Pacific Ocean, the Kelvin wave reaches 4000 m without generating reflected Rossby waves because of the larger basin size. The arrowheads in all panels indicate the direction of the ray paths, and the ray paths are shown only for the first meridional mode except in panel (c).

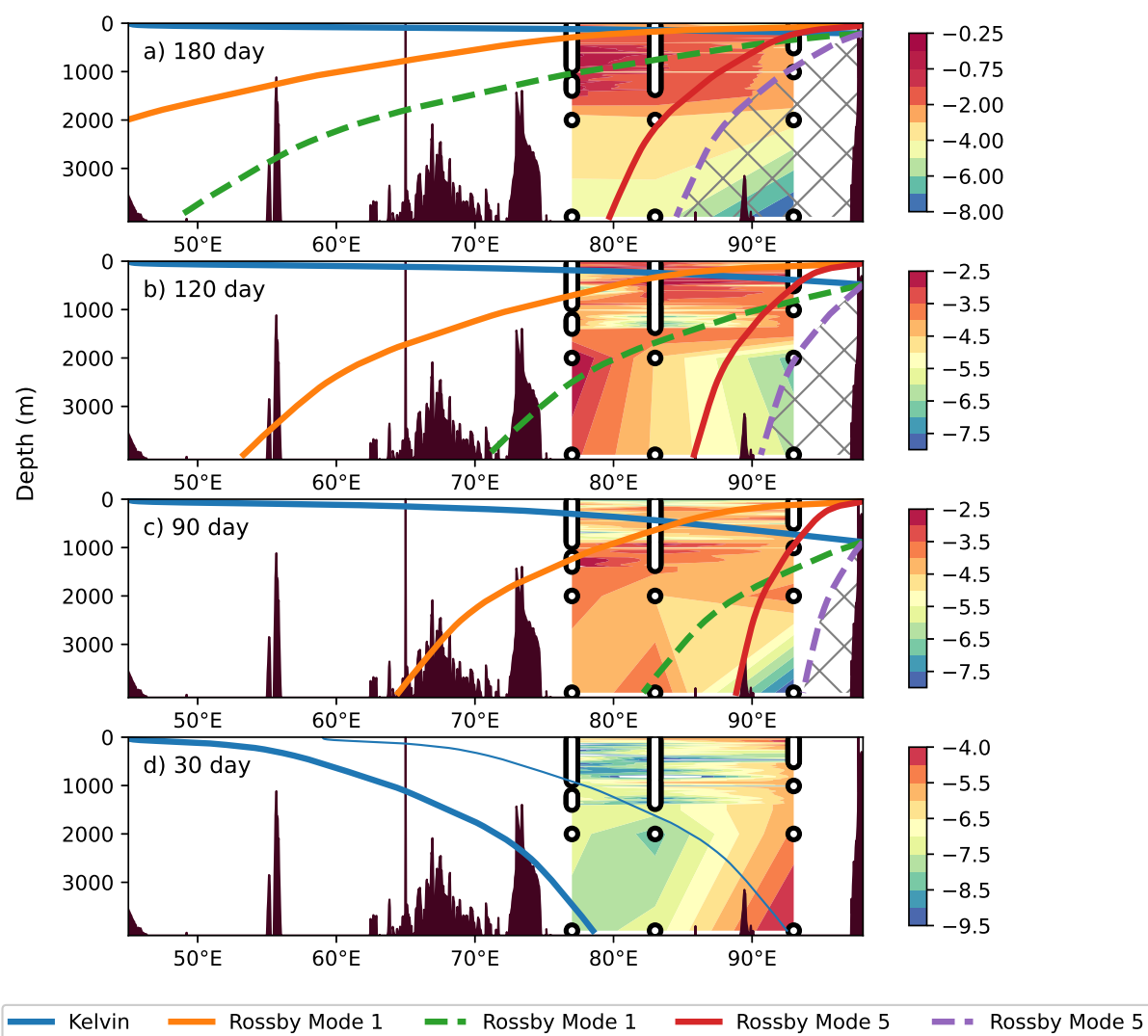


**Fig. 4** The panels show ray paths for Kelvin and Rossby waves for four different periods: a) 180 day, b) 120 day, c) 90 day, and d) 30 day. The shaded color represent the log of the normalized periodogram of the zonal currents. Blue solid (thin) line is the Kelvin ray path generated from the western boundary ( $59.5^{\circ}\text{E}$ ). The orange and red solid lines are Rossby beams generated at the eastern boundary for mode 1 and 5, respectively. The green and purple dashed lines are the Rossby beams generated after the Kelvin wave (blue solid) reflects from the eastern boundary. The dark brown region is the bathymetry and the hatched region is the shadow zone for the mode 5 reflected Rossby waves. The white vertical line/circles show data availability. The lines represent ADCP data and the circles represent data from current meters. The ray paths are calculated based on the WKB theory. The colour levels for the periodogram are not the same for all panels.

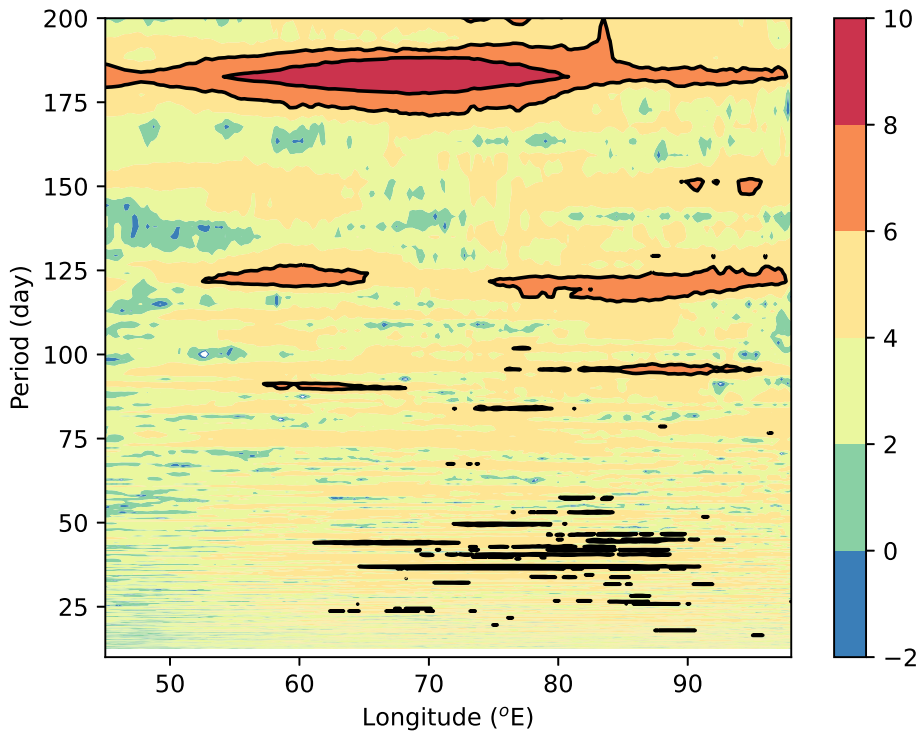


**Fig. 5** Figure showing periodogram of winds at the equator. The power is plotted in log scale after detrending and applying a Hamming window. The ordinate is periods and the abscissa is the longitude. The wind data used to calculate the periodogram extends from 2000–2016.